A Synchronous Piezoelectric–Electromagnetic Hybrid Energy Harvesting Platform With Coil-Sharing Scheme

Wei, Y.; Yue, X.; Lu, T.; Du, S.; Chen, Zhiyuan

DOI
10.1109/JSSC.2025.3619148

Publication date
2025

Document Version
Final published version

Published in
IEEE Journal of Solid-State Circuits

Citation (APA)
Wei, Y., Yue, X., Lu, T., Du, S., & Chen, Z. (2025). A Synchronous Piezoelectric–Electromagnetic Hybrid Energy Harvesting Platform With Coil-Sharing Scheme. *IEEE Journal of Solid-State Circuits*, *60*(12), 4407-4420. https://doi.org/10.1109/JSSC.2025.3619148

A Synchronous Piezoelectric–Electromagnetic Hybrid Energy Harvesting Platform With Coil-Sharing Scheme

Yuchen Wei, Xinling Yue, *Graduate Student Member, IEEE*, Tianqi Lu, *Graduate Student Member, IEEE*, Zhiyuan Chen, *Member, IEEE*, and Sijun Du, *Senior Member, IEEE*

***Abstract*—Vibration energy harvesting is a promising power solution for autonomous wireless sensor nodes, particularly in volume-constrained Internet-of-Things (IoT) applications. Piezoelectric (PE) and electromagnetic (EM) transducers are widely used to convert vibration energy into electrical power. While hybrid PE–EM harvesters can deliver higher output power to support self-sustained systems, existing implementations invariably rely on at least one off-chip inductor for either PE bias-flip or dc–dc conversion, substantially increasing system volume. This article presents an inductor-less, capacitor-less PE–EM hybrid energy harvesting platform that eliminates this limitation. By leveraging the inherent phase synchronization between PE and EM sources, the proposed coil-sharing technique enables both bias-flip and dc–dc conversion without additional passive components, enabling the first fully integrated hybrid energy harvesting system. Fabricated in 0.18-μm CMOS technology, the prototype delivers dual-regulated outputs at 1.8 and 5 V for multi-domain sensor nodes, achieving a maximum output power of 2.72 mW and a peak end-to-end (E2E) efficiency of 90%. These results highlight the platform's potential for ultra-compact, high-performance energy harvesting in next-generation IoT applications.**

***Index Terms*—Coil sharing, electromagnetic (EM) energy harvester, hybrid energy harvesting, kinetic energy, piezoelectric (PE) energy harvester, synchronized switch harvesting on inductor (SSHI).**

I. Introduction

With the rapid advancement of the Internet of Things (IoT), wireless sensor networks (WSNs) are increasingly deployed in applications such as smart homes, environmental monitoring, and implantable electronics [1]. These applications demand higher levels of system integration and reduced maintenance frequency. However, battery (BAT) replacement is often difficult and costly, especially for highly integrated systems or those operating in remote or harsh environments. To address the limitations of BAT lifetime and size, self-sustaining vibration energy harvesting (EH) has emerged as a promising solution [2], as illustrated in Fig. 1. The vibration energy is abundantly available in ambient environments and can be effectively converted into electrical energy using either piezoelectric (PE) or electromagnetic (EM) transducers. Both types of transducers are excited by mechanical vibrations and convert kinetic energy into alternating current (ac) electrical power.

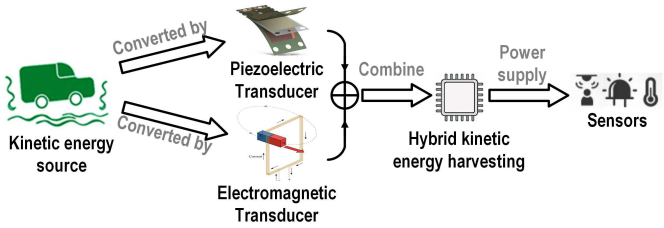

Fig. 1. Kinetic energy harvesting for IoT sensors.

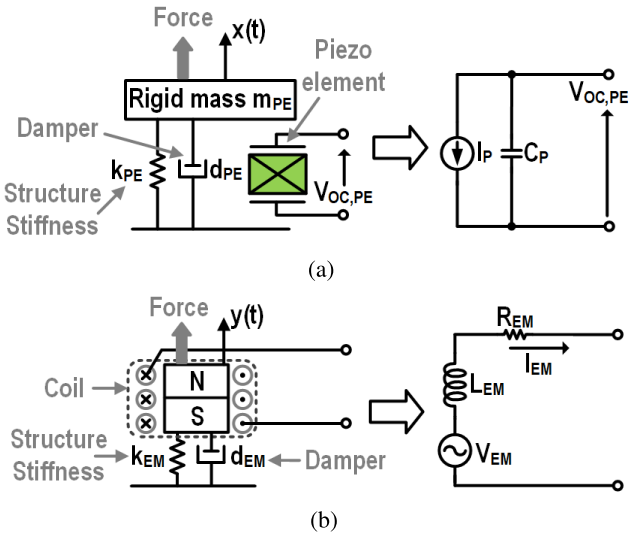

Fig. 2. Equivalent circuit models of energy transducers. (a) Equivalent circuit of a PE transducer. (b) Equivalent circuit of an EM transducer.

Fig. 2 shows the equivalent circuit models of PE and EM transducers. A PE transducer is typically modeled as an ac current source I_P in parallel with its intrinsic capacitance

Received 1 May 2025; revised 10 August 2025 and 18 September 2025; accepted 30 September 2025. Date of publication 23 October 2025; date of current version 3 December 2025. This article was approved by Associate Editor Kousuke Miyaji. *(Yuchen Wei and Xinling Yue contributed equally to this work.) (Corresponding authors: Zhiyuan Chen; Sijun Du.)*

Yuchen Wei, Xinling Yue, Tianqi Lu, and Sijun Du are with the Department of Microelectronics, Delft University of Technology, 2628 CD Delft, The Netherlands (e-mail: sijun.du@tudelft.nl).

Zhiyuan Chen is with the School of Microelectronics, Fudan University, Shanghai 201203, China (e-mail: chen_zy@fudan.edu.cn).

Color versions of one or more figures in this article are available at https://doi.org/10.1109/JSSC.2025.3619148.

Digital Object Identifier 10.1109/JSSC.2025.3619148

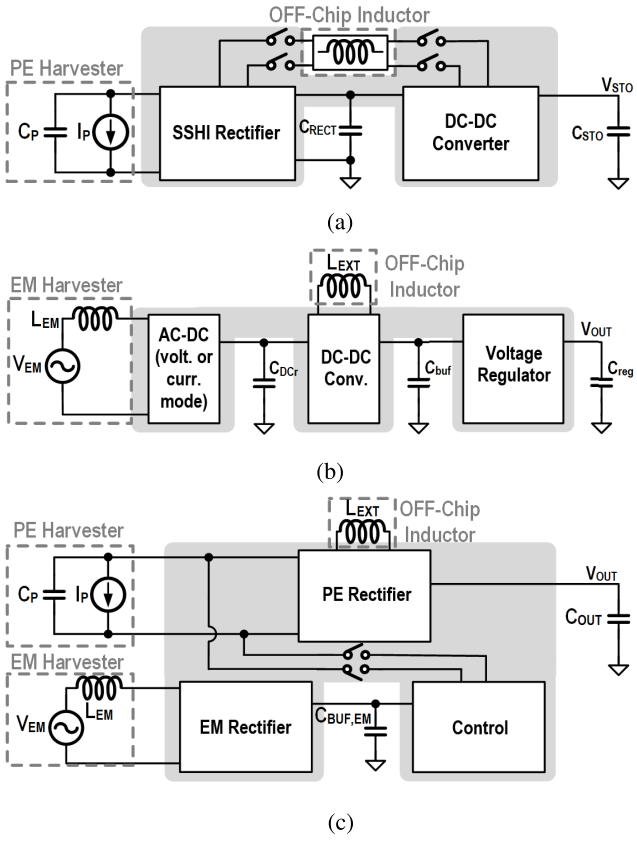

Fig. 3. Conceptual system diagrams of conventional designs. (a) Conventional PE energy harvesting system [3]. (b) Conventional EM energy harvesting system [15]. (c) Conventional PE–EM hybrid energy harvesting system [16].

C_P, while an EM transducer is modeled as an ac voltage source V_{EM} in series with its intrinsic inductance L_{EM} and dc resistance R_{EM}. To enhance energy extraction efficiency, various interface circuits have been developed for both PE and EM EH systems. For PE harvesters, the synchronized switch harvesting on inductor (SSHI) technique—also known as the bias-flip rectifier—is among the most effective methods for addressing charge loss in conventional full-bridge rectifiers (FBRs) [3], [4], [5]. An SSHI rectifier works by actively flipping the residual charge stored in C_P at the zero-crossing moment of I_P. Compared with an FBR, it reduces the charge waste due to self-flipping; hence, the energy extraction performance is significantly increased. A typical PE EH system includes an SSHI rectifier followed by a dc–dc converter for maximum power point tracking (MPPT) [6], [7], [8], [9], as illustrated in Fig. 3(a). While inductor-sharing schemes have been introduced to reduce the number of discrete components, these systems still require at least one off-chip inductor shared between the rectifier and dc–dc stages. Although the use of synchronized switch harvesting on capacitors (SSHCs) allows a fully integrated rectifier by using on-chip capacitors for bias-flipping [10], [11], [12], [13], [14], the dc–dc conversion stage still relies on an off-chip inductor due to the limited voltage conversion ratio and complexity of fully integrated switched-capacitor converters.

In EM energy harvesting systems, rectifiers are generally classified into voltage-mode and current-mode types.

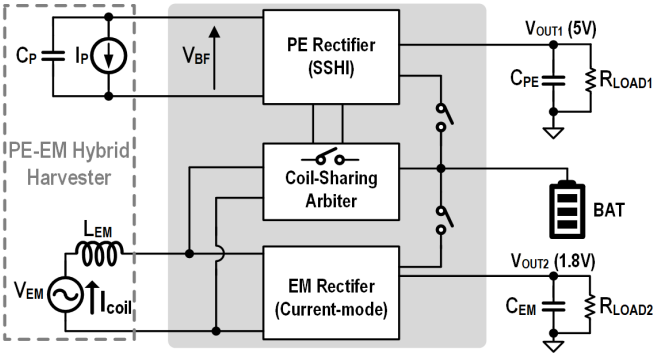

Fig. 4. Proposed coil-sharing PE–EM hybrid energy harvesting system.

Voltage-mode rectifiers often use a negative voltage converter (NVC), which operates similar to an FBR [15]. Current-mode rectifiers, on the other hand, function as boost converters operating in discontinuous conduction mode (DCM), utilizing the EM coil itself as the inductor [17], [18]. A typical EM EH system is shown in Fig. 3(b). Although these systems can eliminate off-chip components in the ac–dc rectifier stage, they still require an off-chip inductor in the dc–dc stage to ensure efficient MPPT and power management [15].

To increase output power and support power-hungry multi-sensor IoT platforms, hybrid EH systems combining both PE and EM transducers have been explored [16], [19], [20], [21], [22], [23]. A typical PE–EM hybrid system is shown in Fig. 3(c). Although these designs reduce the number of off-chip inductors to one, shared across PE bias-flip, dc–dc conversion, and output regulation, this remaining inductor still prevents full system integration. Furthermore, most existing systems only support a single regulated output, which limits their applicability for modern sensor nodes that require multiple voltage domains.

To overcome these limitations, this article proposes a coil-sharing scheme that enables fully integrated hybrid PE–EM energy harvesting with dual-regulated outputs [24]. By exploiting the in-phase relationship between the voltage across the EM transducer and the current through the PE transducer, the proposed technique eliminates the need for any off-chip or on-chip inductors or capacitors for power conversion. As a result, the system reduces volume while achieving high energy extraction efficiency, making it suitable for compact, multi-rail energy harvesting applications.

The remainder of this article is organized as follows. Section II introduces the working principle of the proposed coil-sharing scheme, the hybrid PE–EM energy transducer, and operational modes. Section III presents the system architecture and system-level operations. Section IV details the circuit implementation. Measurement results are provided in Section V, and the conclusion is drawn in Section VI.

II. Proposed Hybrid EH Platform

A. Coil-Sharing Scheme Concept

This work proposes a fully integrated PE–EM hybrid energy harvesting platform employing a novel coil-sharing scheme, as shown in Fig. 4. The external discrete components

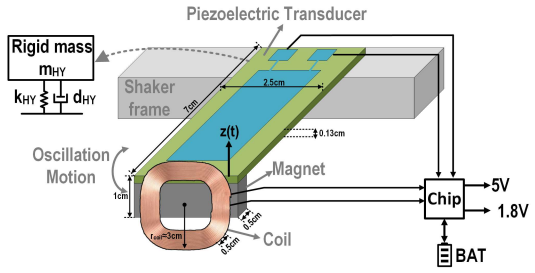

Fig. 5. Hybrid PE–EM energy transducer designed in this work.

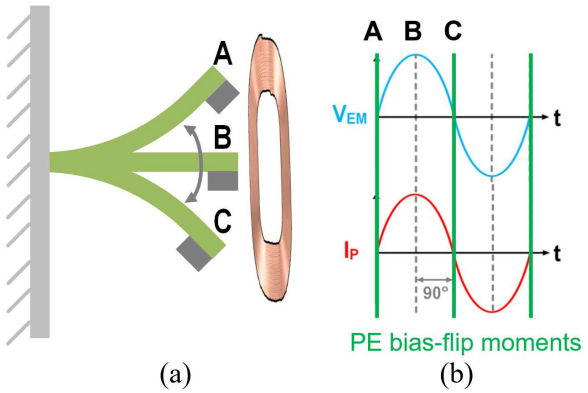

Fig. 6. (a) Side view of the proposed hybrid PE and EM transducer. (b) Phase relationship between PE and EM transducers.

include a hybrid PE–EM energy transducer, two off-chip buffer capacitors (C_{PE} and C_{EM}) for regulated outputs (V_{OUT1} = 1.8 V and V_{OUT2} = 5 V), and a BAT or supercapacitor for energy storage. The integrated chip includes a PE rectification block, an EM rectification block, and a coil-sharing controller that dynamically reassigns the EM coil for different roles.

The PE–EM transducer co-locates PE and EM energy transducers, which generate phase-synchronized outputs. During typical operation, the PE source is rectified through an SSHI interface to generate the 5-V output (V_{OUT1}), while the EM coil operates as an active transducer, rectified via a multi-step current-mode rectifier to supply the 1.8-V output (V_{OUT2}).

At the zero-crossing of I_P, the SSHI rectifier requires an inductor to form an *LC* resonant loop that flips the PE voltage V_{BF} across C_P. At this point, the EM coil is repurposed as a bias-flip inductor, connected in parallel with C_P. Under light load conditions, excess energy from both PE and EM sources is stored in the BAT. Because the current paths to the output capacitors (C_{PE} and C_{EM}) run in parallel with those to the BAT, no cascaded energy loss occurs. Under heavy load, internal buck–boost dc–dc paths transfer BAT energy to the two output capacitors, with the EM coil reused as a dc–dc inductor.

To achieve all the above-mentioned operations, the EM coil needs to work correctly in three different roles.

1) EM energy source.
2) PE bias-flipping inductor. DC–DC.
3) power conversion inductor.

B. Transducer Design and Coil Role Feasibility

To support all three roles, the hybrid PE–EM transducer and supporting control circuitry were co-designed. Fig. 5 shows the transducer: a magnet is mounted at the free end of a PE cantilever, with an EM coil fixed in front. When subjected to ambient vibrations, the cantilever oscillates vertically. The PE effect generates voltage across the cantilever electrodes, while the moving magnet induces voltage in the EM coil. Both signals are fed into the chip for energy extraction. The dimensions of each component are included in Fig. 5. The overall volume of the fabricated transducer is 17.6 cm^3. The coil radius is designed to cover the vertical displacement range of the magnet in order to effectively capture the full magnetic flux. In PE energy harvesting systems, a proof mass is commonly attached to the beam end [25] to increase cantilever deflection and strain, thereby enhancing the electrical output. It also lowers the resonant frequency of the system, improving its efficiency for low-frequency ambient vibrations. In this work, the magnet mass effectively serves as the proof mass of the PE cantilever. For practical applications, both the cantilever dimensions and the magnet mass can be customized to tune the resonant frequency to match the dominant low-frequency vibrations encountered in real environments.

1) Role 1 (EM Energy Source): This is the coil's original function. Vibrations induce voltage across the coil, validating its operation as an EM transducer. In this work, a current-mode rectifier extracts this energy and delivers it to the regulated outputs.

2) Role 2 (PE Voltage Bias-Flipping Inductor): To evaluate the feasibility of the second role, a critical assumption must hold: the instantaneous energy stored in the EM coil must be 0, i.e., V_{EM} = 0, at the moment it is used for PE bias-flipping. This ensures that the coil's internal energy does not interfere with the voltage-flipping operation across C_P, thereby preserving the intended bias-flipping behavior.

Fig. 6(a) shows the side view of the proposed hybrid PE–EM energy transducer, which indicates three key positions when the structure is vibrating: A–C. Position B is the equilibrium position, where the cantilevered structure has zero displacement and the maximum velocity. In contrast, at positions A and C, the cantilever has the maximum displacement and zero velocity.

For the PE transducer, based on the PE effect, the generated current is proportional to the time derivative of the mechanical strain. In other words, the faster the strain changes in the PE element, the greater the resulting current. For the EM transducer, according to Faraday's law of EM induction, the induced electromotive force (EMF) is proportional to the time derivative of the magnetic flux.

Therefore, when the magnet reaches position B (the equilibrium point with maximum velocity), the rates of strain change in the PE element and magnetic flux change in the EM coil are both maximized. As a result, position B corresponds to the peak values of both the PE-induced current, I_P, and the EM-induced voltage, V_{EM}. In contrast, at positions A and C, where the cantilever displacement is maximal but velocity is 0, both

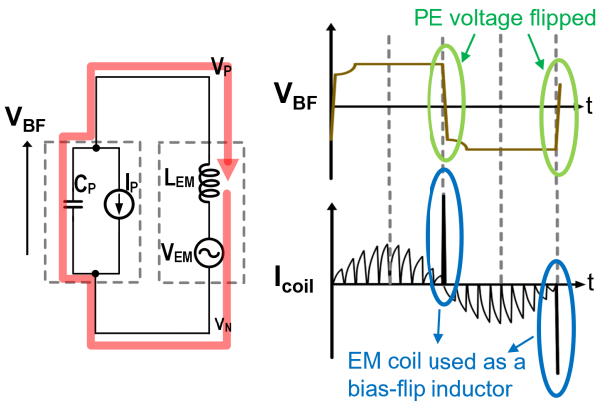

Fig. 7. Operation when the EM coil is used as a PE bias-flipping inductor.

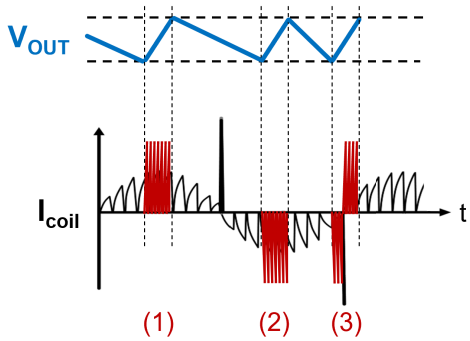

Fig. 8. Operation waveform when the EM coil is used as a dc–dc inductor.

the strain change rate and the magnetic flux change rate fall to 0. Consequently, these positions align with the zero-crossing points of I_P and V_{EM}.

The time-domain waveforms of I_P and V_{EM} during vibration can therefore be expressed as follows:

$$I_P = I_{P0} \sin(\omega t) \tag{1}$$

$$V_{EM} = V_{EM0} \sin(\omega t) \tag{2}$$

where I_{P0} is the I_P current amplitude, V_{EM0} is the V_{EM} voltage amplitude, and ω is the angular frequency of the vibration. For the PE transducer, its open-circuit voltage, $V_{OC,PE}$, can be expressed as follows:

$$V_{OC,PE} = -\frac{I_{P0}}{\omega C_P} \cos(\omega t). \tag{3}$$

Equations (1)–(3) confirm that V_{EM} and I_P are in phase, while $V_{OC,PE}$ lags by 90°, as shown in Fig. 6(b). In the context of PE energy harvesting, bias-flipping occurs at the zero-crossing points of I_P, which correspond to positions A and C. Notably, at these moments, $V_{EM} = 0$, indicating that the EM coil holds no initial energy. This unique alignment, enabled by the transducer's mechanical and electromechanical design, makes the EM coil ideally suited for Role 2, as a PE voltage bias-flipping inductor.

During the bias-flipping moment, the EM coil is connected in parallel with the PE harvester, as shown in Fig. 7. The sharp spikes observed in the coil current, I_{coil}, confirm that the coil functions as an inductor during this phase. When not serving as a bias-flipping inductor, the coil operates as an energy source, and its harvested energy is extracted through a current-mode rectifier, which will be detailed later.

3) Role 3: Dc–Dc Power Conversion Inductor: Under heavy loading conditions, the harvested energy from the PE and EM transducers may not be sufficient to sustain V_{OUT1} and V_{OUT2}. In such cases, the BAT supplements the system through a dc–dc conversion path, with the EM coil repurposed as the inductor to assist in maintaining output regulation.

During this process, a critical condition must be satisfied: the energy already harvested and stored in the EM transducer should not be wasted. To ensure this, a coil-polarity-matching (CPM) technique is introduced. The CPM aligns the direction of the dc–dc current with that of the intrinsic EM-induced current in the coil. This alignment allows the harvested EM energy to be preserved and efficiently delivered to the output, in tandem with the BAT-assisted dc–dc operation.

Fig. 8 illustrates the waveforms of V_{OUT} and I_{coil} during this process, where V_{OUT} (V_{OUT1} or V_{OUT2}) cannot be sustained by harvested energy alone. Once V_{OUT} reaches the lower boundary of the hysteresis window, the dc–dc operation begins. Three scenarios can occur depending on the instantaneous direction of I_{coil}.

1) *Case 1:* When I_{coil} is positive, the coil is connected such that the dc–dc current flows in the same direction.
2) *Case 2:* When I_{coil} becomes negative, the coil connection is flipped to maintain alignment between the dc–dc and intrinsic coil currents.
3) *Case 3:* Within a single dc–dc event, I_{coil} may change direction. In this case, the CPM technique dynamically flips the coil connection as soon as a polarity reversal is detected.

To support real-time polarity detection in case 3, the system leverages the existing PE bias-flipping signal as a timing reference. Since this signal inherently coincides with the zero-crossing comment of the EM-induced voltage, it serves as an effective and energy-efficient trigger for reversing the coil connection.

4) Priority of the Three Roles: Since the EM coil serves three distinct roles, it is crucial to establish its access priorities. The highest priority is given to the PE bias-flipping (Role 2), as this operation must occur precisely at the zero-crossing point of I_P. If missed, the performance of PE energy harvesting would be significantly compromised.

The second priority is the dc–dc power conversion (Role 3). During this phase, the harvested energy stored in the EM coil is efficiently transferred to the output, thanks to the CPM technique, which ensures that the EM energy is not wasted.

The lowest priority is assigned to the EM energy source (Role 1). However, this does not imply that the EM-harvested energy is wasted. During PE bias-flipping, the instantaneous EM energy in the coil is negligible ($V_{EM} \approx 0$). When dc–dc conversion occurs, the EM-harvested energy is effectively transferred to the outputs as well.

Thus, the designed priority system ensures efficient utilization of the EM coil across all its roles, optimizing the overall energy harvesting process.

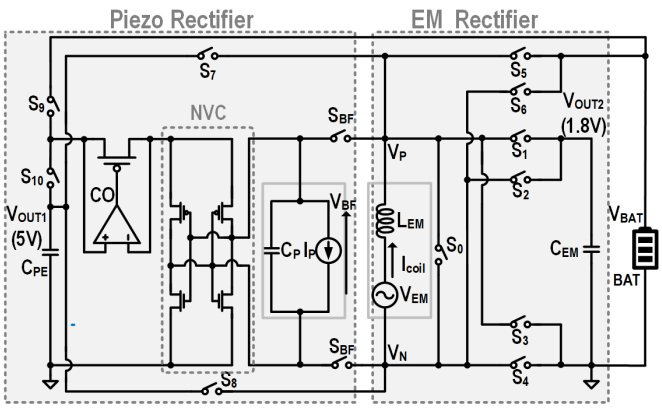

Fig. 9. Power stage of the proposed coil-sharing scheme.

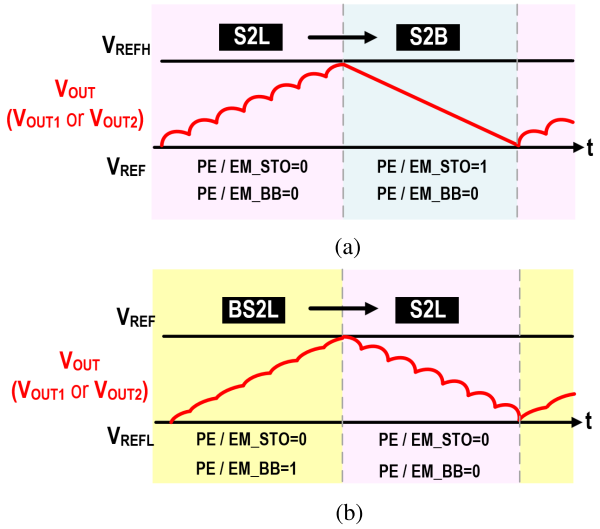

Fig. 10. Three operation modes for different loading conditions. (a) Light loading condition ($P_{harvested} > P_{load}$). (b) Heaving loading condition ($P_{harvested} < P_{load}$).

It is worth noting that most EM harvesters require a coil in the mH range to generate sufficient induced energy [15], [16], [26]. An inductance of this magnitude avoids the excessive current peaking that would occur with an extremely small inductance during the PE bias-flipping resonance, thereby reducing instantaneous stress on the coil and series switches; while scalable-N SSHI can mitigate this low-L/low-Q issue [4], our architecture does not rely on it. Conversely, if the EM coil inductance becomes very large, the longer LC flip duration can begin to overlap with normal EM energy extraction at the ambient vibration frequency. A practical approach is to partition the coil into several reconfigurable sections that remain series-connected during normal EM operation, and at the EM phase-changing point (which coincides with the PE bias-flip instant), selectively connect a middle sub-coil of relatively small inductance in parallel with the PE transducer to perform the flip of V_{PE}. This way, the sub-coil inductance sets a short, well-controlled flip time that stays small relative to the ambient vibration period, while the full-coil inductance is preserved for efficient EM harvesting. Furthermore, MPPT techniques [9], [27], [28] can be incorporated to further enhance the overall energy harvesting efficiency over varying vibration levels.

C. Proposed Power Stage Topology

The proposed power stage is shown in Fig. 9. It consists primarily of a PE SSHI rectifier, an EM current-mode rectifier, and embedded dc–dc paths. In the center of the topology are the electrical models of the proposed hybrid PE–EM energy transducer, incorporating synchronized PE and EM energy transducers. Each of the two outputs, V_{OUT1} and V_{OUT2}, is regulated by a three-threshold double-window hysteresis controller, with a 100-mV hysteresis window among V_{REFH}, V_{REF}, and V_{REFL} (V_{REF} is 5 V for V_{OUT1} and 1.8 V for V_{OUT2}), as shown in Fig. 10. Since the regulation strategy is the same for both outputs, we use the term V_{OUT} to refer to either V_{OUT1} or V_{OUT2} in the following discussion.

Under light loading conditions, when the harvested power exceeds the load power ($P_{harvested} > P_{load}$), the output V_{OUT} is sustained solely by the harvested energy, regulated within the upper hysteresis window between V_{REF} and V_{REFH}. On the other hand, if the harvested power is insufficient to meet the load demand ($P_{harvested} < P_{load}$), V_{OUT} will drop below V_{REF}, and the system will regulate it within the lower hysteresis window between V_{REFL} and V_{REF}.

The system operates in one of three modes depending on the loading conditions: source-to-load (S2L) mode, source-to-battery (S2B) mode, and battery-and-S2L (BS2L) mode. In light loading conditions, as illustrated in Fig. 10(a), the harvested power is greater than the load, so the harvested energy from the PE or EM source first sustains the load (S2L period), and any excess energy is stored in the BAT (S2B period). Under heavy load conditions, as shown in Fig. 10(b), the harvested energy is insufficient to meet the load (S2L period), so the BAT provides additional power, together with the harvested energy in the EM source, to sustain V_{OUT} (BS2L period). The current paths for each of these operation modes are shown in Fig. 11. To minimize conduction loss, the power stage is designed to ensure that not more than two power switches are cascaded on a single current path at any time. Fig. 11(a) illustrates the PE voltage (V_{BF}) bias-flipping path, which was introduced in Fig. 7, and the operations of all three modes are detailed below.

1) S2L Mode: This mode occurs under both light and heavy loading conditions. In this mode, the harvested energy is directly supplied to the load. Fig. 11(b) shows the power path in S2L mode from the PE energy harvester when the PE voltage is positive. The PE energy is transferred to the output capacitor C_{PE} via an NVC for both positive and negative PE voltage polarities. When the PE voltage is negative, the alternative path of the NVC becomes active.

Fig. 11(c) shows the S2L power path to charge V_{OUT2} from the EM energy source when $V_{EM} > 0$. The current-mode multi-step rectifier operates in two phases. In phase 1, switch S_0 is closed, and the EM current energizes the coil. In phase 2, S_0 opens while S_1 and S_4 are closed,

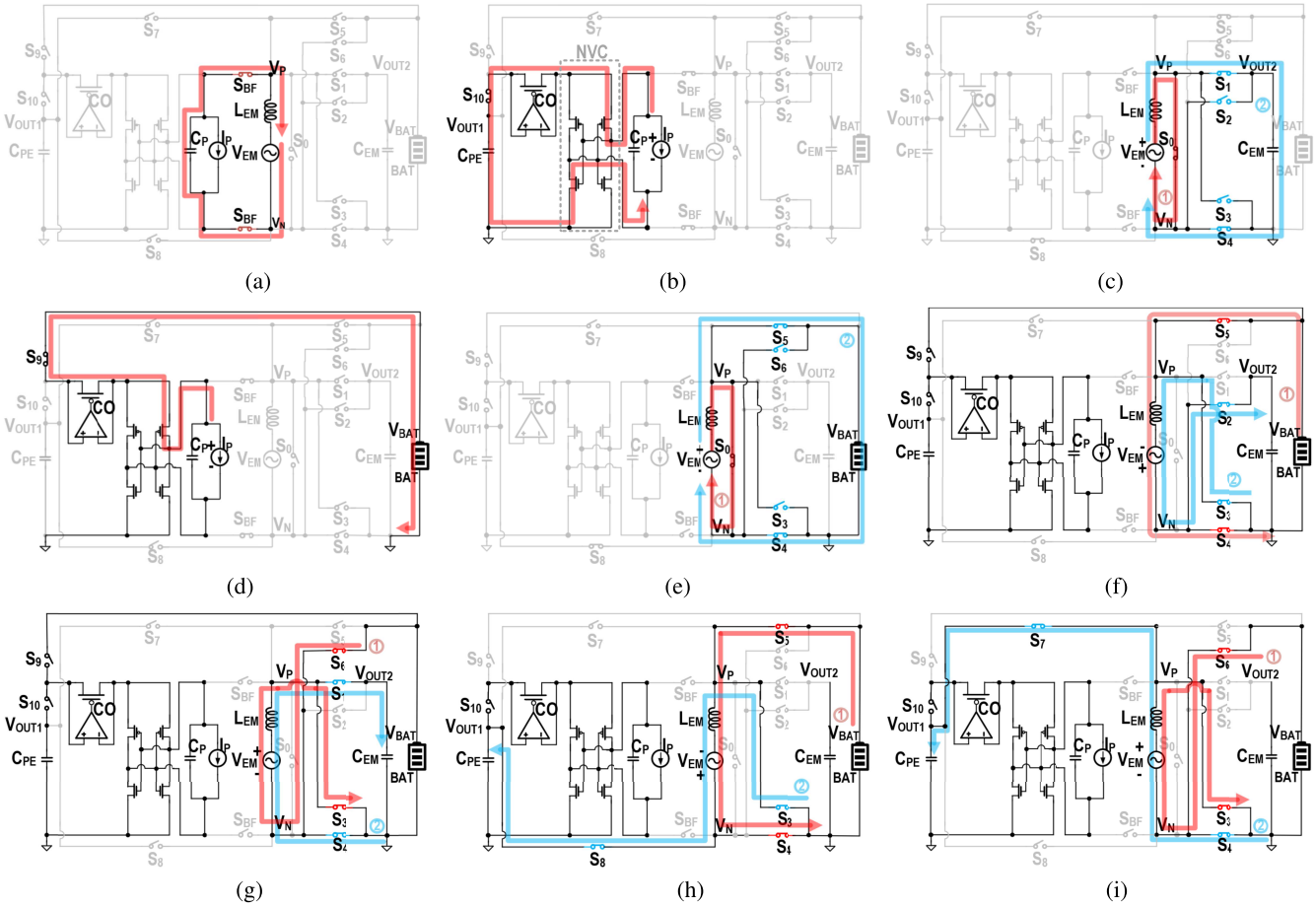

Fig. 11. Power paths for different operation modes. (a) PE bias-flipping. (b) S2L for PE (positive). (c) S2L for EM (positive). (d) S2B for PE (positive). (e) S2B for EM (positive). (f) BS2L Path-1 (neg. I_{coil} to V_{OUT2}). (g) BS2L Path-2 (pos. I_{coil} to V_{OUT2}). (h) BS2L Path-3 (neg. I_{coil} to V_{OUT1}). (i) BS2L Path-4 (pos. I_{coil} to V_{OUT1}).

de-energizing the coil and charging capacitor C_{EM}, similar to a boost conversion operation. When $V_{EM} < 0$, phase 1 remains unchanged, but in phase 2, switches S_2 and S_3 are activated instead.

2) S2B Mode: This mode is activated only under light loading conditions, when there is excess harvested energy after sustaining the output. As shown in Fig. 10(a), this mode is enabled when V_{OUT} naturally decreases from V_{REFH} to V_{REF} due to the load. The rectification principles and power paths are similar to the S2L mode, but the excess energy is transferred to the BAT rather than the output capacitors.

Fig. 11(d) shows the S2B power path from the PE harvester to the BAT when the PE voltage is positive. Fig. 11(e) shows the S2B power path from the EM source when $V_{EM} > 0$. Similar to the S2L mode, this mode consists of two sub-phases: the coil-energizing phase and the BAT-charging phase. When $V_{EM} < 0$, switches S_2 and S_3 are activated to match the polarity of the current.

3) BS2L Mode: This mode is activated only under heavy load conditions, when the BAT is required to assist in charging and sustaining V_{OUT} via dc–dc buck–boost conversion. As previously discussed, the EM coil current I_{coil} must align with the dc–dc current. Therefore, four distinct power paths are defined, depending on the polarity of I_{coil} and the output voltage (V_{OUT1} and V_{OUT2}), as shown in Fig. 11(f)–(i). Each of these paths consists of two sub-phases. First, the coil is energized using BAT power, and then, the energy stored in the coil is used to charge one of the outputs, similar to a buck–boost conversion.

Table I summarizes the four BS2L dc–dc power paths, along with the corresponding control signals, activated switches, and conditions.

III. System Architecture

Fig. 12 illustrates the top-level system architecture of the proposed hybrid PE-EM energy harvesting platform with the coil-sharing scheme. The system comprises a power stage, an SSHI rectifier controller, an EM rectifier controller, a dc–dc controller, and an output regulation block. The power stage includes several power switches, with the operational principles detailed in Section II-C. The hybrid PE–EM energy transducer, along with two off-chip capacitors (C_{PE} and C_{EM}) and a BAT, provides the necessary energy storage. A maximum voltage selector is used to select the higher voltage between V_{BAT} and V_{OUT1} to power the entire system.

The output regulation block uses two three-threshold hysteresis comparators, one for each output, to monitor the

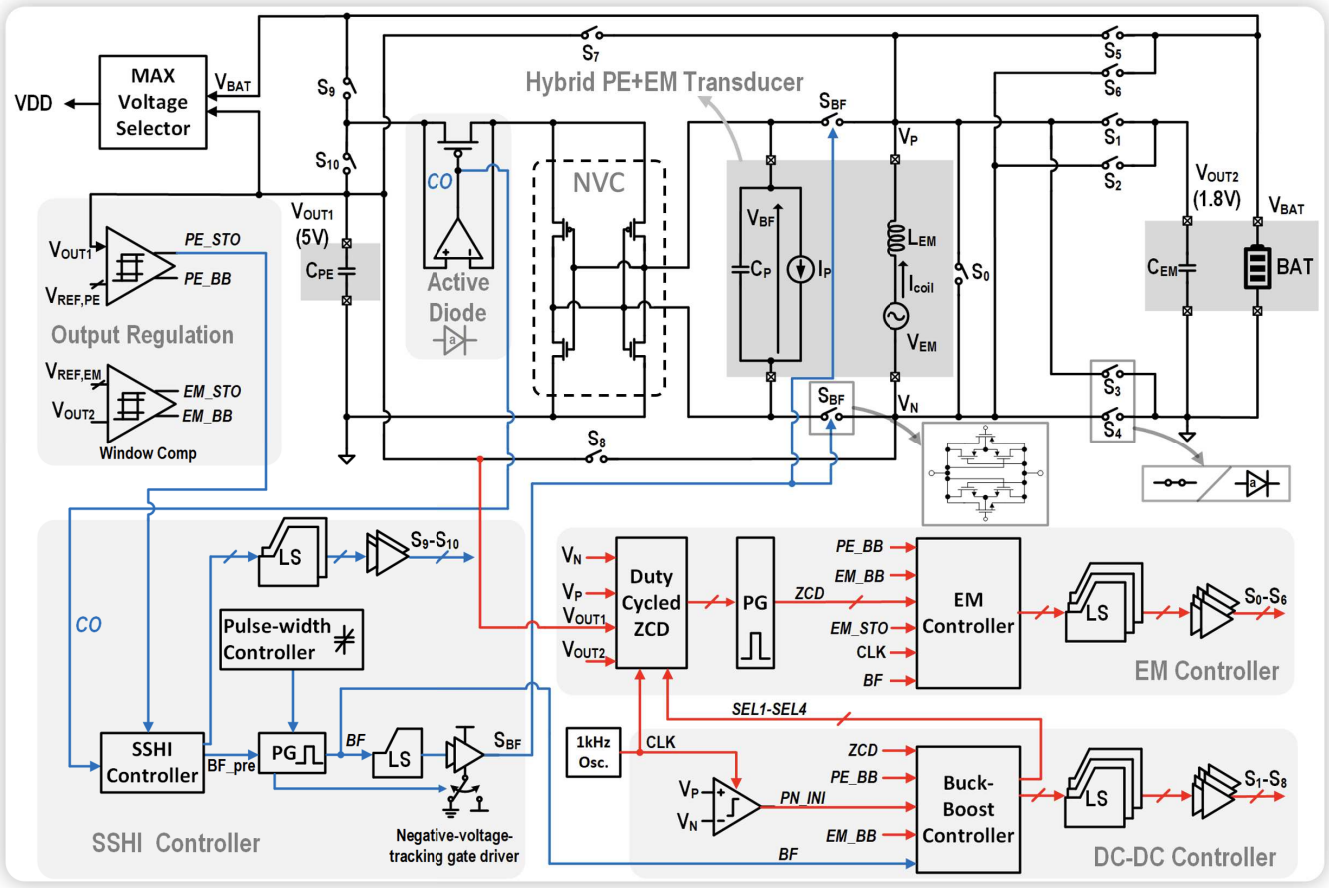

Fig. 12. System architecture of the proposed coil-sharing hybrid energy harvesting platform.

TABLE I
OPERATION SUMMARY OF FOUR BS2L DC–DC PATHS

BS2L DC-DC Paths	Selecting Signals	Activated Switches	EM Polarity	Output charged
Path 1	*SEL1*	Phase 1: S_4, S_5 Phase 2: S_2, S_3	Neg. EM half-cycle	V_{OUT2} (C_{EM})
Path 2	*SEL2*	Phase 1: S_3, S_6 Phase 2: S_1, S_4	Pos. EM half-cycle	V_{OUT2} (C_{EM})
Path 3	*SEL3*	Phase 1: S_4, S_5 Phase 2: S_3, S_8	Neg. EM half-cycle	V_{OUT1} (C_{PE})
Path 4	*SEL4*	Phase 1: S_3, S_6 Phase 2: S_4, S_7	Pos. EM half-cycle	V_{OUT1} (C_{PE})

loading conditions. Based on these conditions, the comparators generate control signals that are sent to the EM controller and the dc–dc controller to manage the system's mode of operation.

The SSHI controller detects the signal CO, which initiates the PE bias-flipping operation. This signal is generated by an active diode, which indicates whether the NVC is conducting. Upon detecting the rising edge of CO, corresponding to the zero-crossing of I_P, a pulse generator (PG) triggers the generation of a control signal *BF*. This signal activates the two power switches S_{BF} via a level shifter and driver. When the switches S_{BF} are on, the PE harvester is connected in parallel with the EM coil, allowing the PE voltage, V_{BF}, to be flipped. The upper path in the SSHI controller generates two drive signals to turn off power switches S_9 and S_{10}, effectively disconnecting the PE harvester from C_{PE} and BAT to ensure a proper bias-flipping operation. Adaptive body biasing technique [4], [11] is also used to further enhance the switch conductance and multiple quadrants operation.

In the EM controller and dc–dc controller, an on-chip oscillator (OSC) generates a 1-kHz clock signal, CLK, to drive the multi-step current-mode EM rectifier and a clocked comparator in the dc–dc controller. To prevent reverse current in the dc–dc paths, a duty-cycled zero-current detector (ZCD) within the EM controller monitors the voltage difference across the two terminals of the high-side switches in the embedded buck–boost converters. Both the EM and dc–dc controllers receive mode-selection signals from the output regulation block, which indicate the current loading conditions. Based on these inputs, the controllers determine the appropriate operating mode and power path, and subsequently generate the corresponding gate-driving signals for the power stage via level shifters and switch drivers. In the proposed system, the maximum value of V_{BAT} is limited to 5.1 V to ensure the safe operation and prevent transistor breakdown.

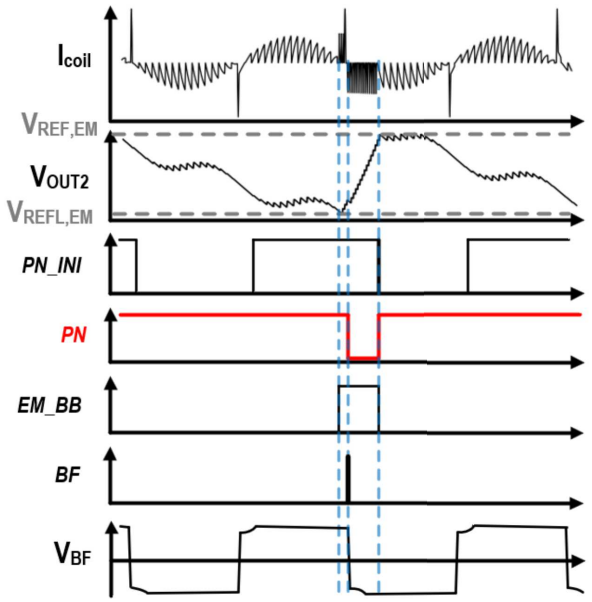

Fig. 13. Timing diagram illustrating the system working behavior under heavy load conditions.

IV. Circuit Implementations

A. Buck–Boost Controller for Embedded Dc–Dc Paths

Fig. 13 presents the waveform illustrating the system behavior under heavy load conditions. Since both outputs follow the same regulation strategy, the EM branch is used as an example. When the output voltage V_{OUT2} reaches the lower hysteresis threshold $V_{REFL,EM}$, the signal EM_BB is asserted high. This signal, generated by the window comparator in the output regulation block, determines the system's operating mode: setting EM_BB = 1 enables the BS2L mode, while EM_BB = 0 indicates S2L mode. For the PE branch, this same function is carried out by the signal PE_BB.

Once either EM_BB or PE_BB is asserted, the buck–boost conversion process is triggered. The EM coil is then assigned to serve as the dc–dc inductor, and the enable signal *EN* activates the dc–dc PG, as shown in Fig. 14(a). The PG subsequently generates two non-overlapping control signals—charging pulse SPC and discharging pulse SPD—as illustrated in Fig. 14(b). These signals are routed to the appropriate power switches by the SW allocation block.

Fig. 14(c) shows the circuit implementation of the direction arbiter within the buck–boost controller. To ensure that the dc–dc current direction aligns with the polarity of V_{EM}, a clocked comparator (CMP_PN, also shown in Fig. 12) monitors the coil current polarity during S2L operation. This comparator generates an initial polarity signal, PN_INI, which is fed into the direction arbiter. Based on PN_INI, the direction arbiter produces one of the four path-selection signals, SEL1–SEL4, depending on the current loading condition, V_{EM} polarity, and coil access request. These signals determine the appropriate BS2L dc–dc path from Table I and are passed to the SW allocation block, which then generates

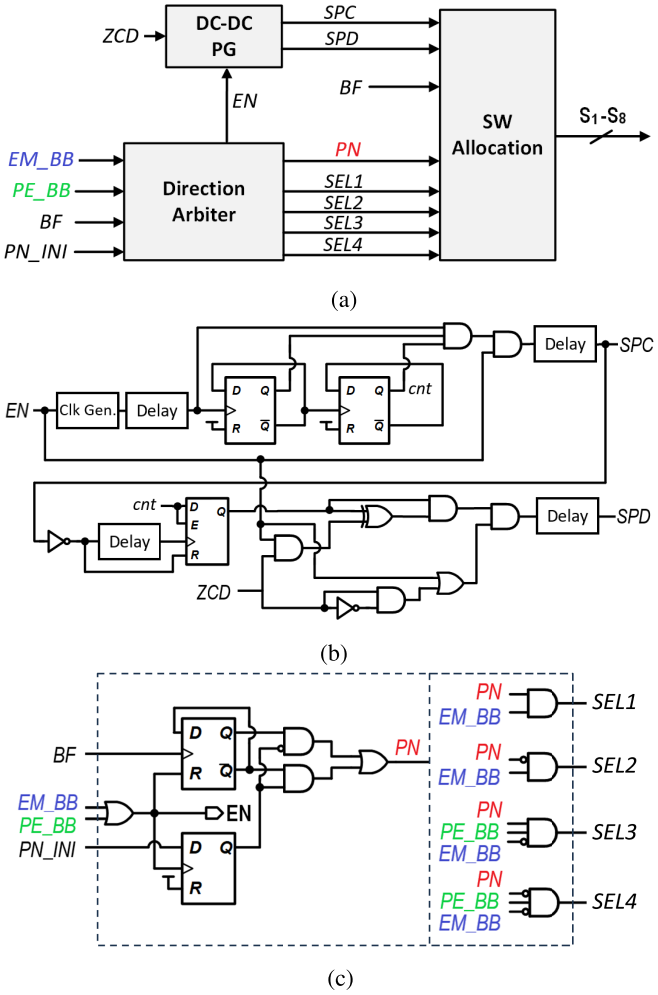

Fig. 14. Circuit diagrams of the buck–boost controller and associated key sub-blocks. (a) Buck–boost controller. (b) DC–DC PG. (c) Direction arbiter.

the corresponding gate-driving signals (S_1–S_8) for the power stage.

As previously discussed, if the dc–dc operation spans two adjacent EM half-cycles with opposite polarities (as in case 3 of Fig. 8), the comparator becomes temporarily inactive, since the EM coil is already engaged as a dc–dc inductor and thus cannot be monitored for polarity. However, due to the synchronous phase relationship between the PE and EM harvesters, the PE bias-flip event always coincides with the zero crossing of V_{EM}. Therefore, the bias-flip signal *BF* can be used as a reliable timing reference to flip the coil polarity.

This condition is clearly illustrated in Fig. 13. At the beginning of each BS2L cycle, the comparator CMP_PN provides the EM polarity to the direction arbiter in the form of the initial signal PN_INI. The arbiter uses this to align the real-time polarity signal *PN* with the target output capacitor and generates the corresponding selection signals SEL1–SEL4. When a *BF* signal is detected—indicating a reversal in the EM-induced voltage—the polarity signal *PN* is flipped, prompting the arbiter to switch to the opposite coil connection path after PE bias-flipping ends.

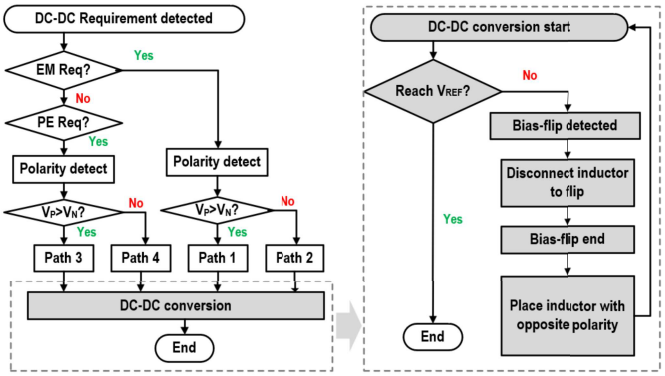

Fig. 15. Working flow of the dc–dc conversion in BS2L mode.

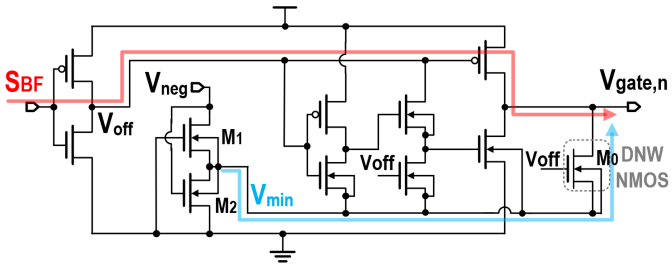

Fig. 16. Negative-voltage-tracking gate driver.

The complete decision process for the dc–dc conversion is summarized in the working flow diagram shown in Fig. 15.

B. Negative-Voltage-Tracking Gate Driver

At the beginning of each EM rectifier phase 2, the current stored in the coil during phase 1 flows into the energy storage element due to inductive freewheeling. During this freewheeling phase, the voltage at node V_N (or V_P) may momentarily drop below ground, typically for a few microseconds. To prevent unintended channel conduction of the NMOS in the transmission gate S_{BF}, which could occur if the gate voltage falls below $-V_{TH,N}$, a body-biased negative-voltage-tracking gate driver is employed, as shown in Fig. 16. This circuit adaptively biases the NMOS gate of S_{BF} according to the lowest system voltage.

The input V_{neg} is connected to the potentially negative node adjacent to the NMOS device. When the control signal for S_{BF} is high, the red path in Fig. 16 is active, and the circuit operates as a conventional buffer to drive the gate. When S_{BF} is low, the deep n-well transistors M_1 and M_2 form a cross-coupled pair that outputs the lower of V_{neg} and GND as V_{min} from the bulk terminal. This value is then passed through M_0, configured as a voltage follower along the blue path, to bias the NMOS gate at $V_{gate,n}$. This ensures that the NMOS remains fully turned off, even in the presence of a transient negative voltage spike.

C. Maximum Voltage Selector

To ensure the system maintains a sufficient supply voltage during start-up or under extremely heavy load conditions, a maximum voltage selector is implemented, as shown in Fig. 17. This circuit selects the higher voltage between V_{BAT} and V_{OUT1}, and outputs it as V_{DD}, which powers the entire system.

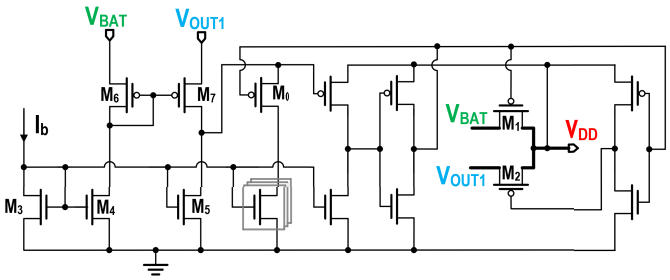

Fig. 17. Maximum voltage selector for the system power supply.

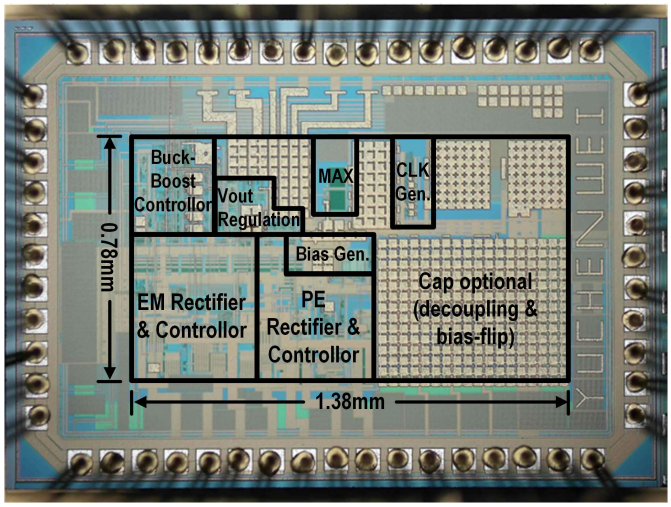

Fig. 18. Chip micrograph.

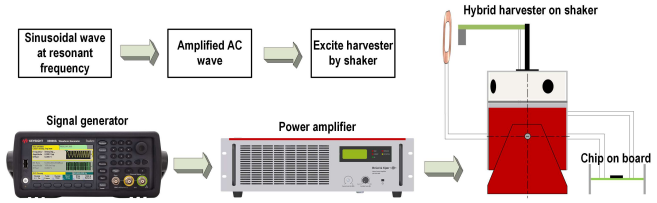

Fig. 19. Experimental setup for vibration testing.

In this design, V_{BAT} and V_{OUT1} are first compared using a common-gate comparator formed by transistors M_4–M_7. Based on the comparison result, control logic drives the power switches M_1 and M_2, allowing the higher of the two input voltages to be passed through as V_{DD}.

V. Measurement Results and Discussion

The fabricated chip micrograph is shown in Fig. 18. The proposed circuit was fabricated in a 0.18-μm CMOS process with a total active chip area of 1.08 mm^2, including decoupling capacitors. The custom hybrid energy harvester was developed in-house, comprising a PE cantilever, an NdFeB magnet, and a hand-wound 2.5-mH coil with approximately 4.5-Ω dc resistance. All measurements were conducted at the harvester's resonant frequency of 30 Hz. As shown in Fig. 19, the

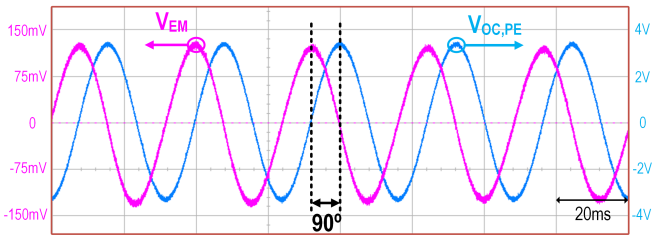

Fig. 20. Measured V_{PE} and V_{EM} waveform.

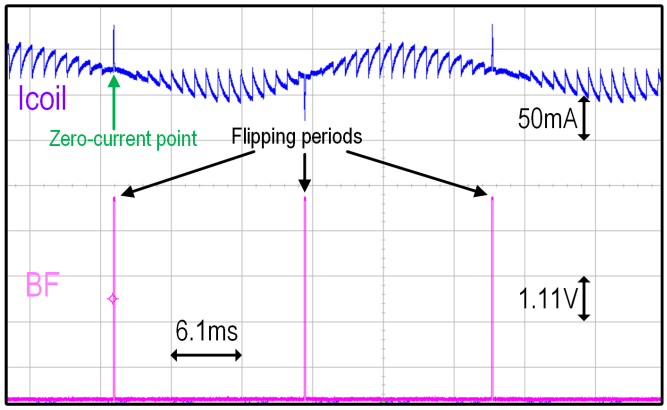

Fig. 21. Measured time-interleaved EM harvesting and PE bias-flip waveform.

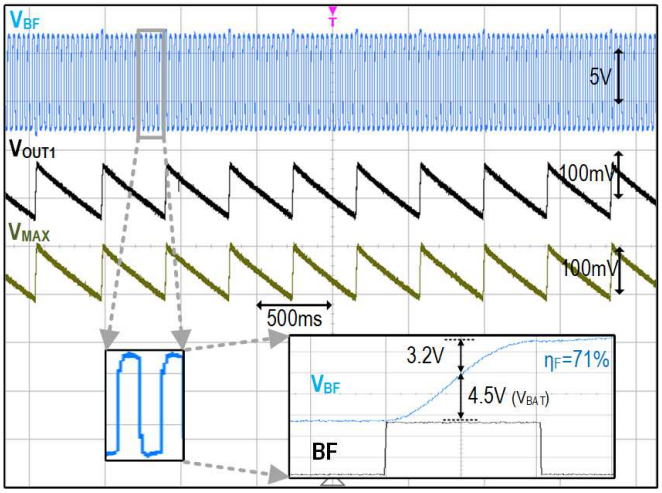

Fig. 22. Measured PE rectifier operation waveform.

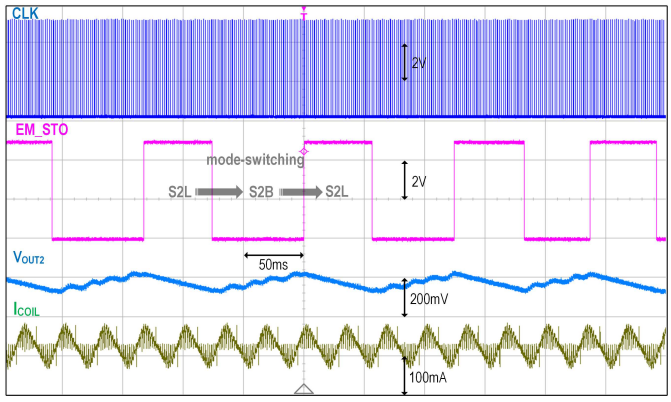

Fig. 23. Measured EM rectifier operation waveform.

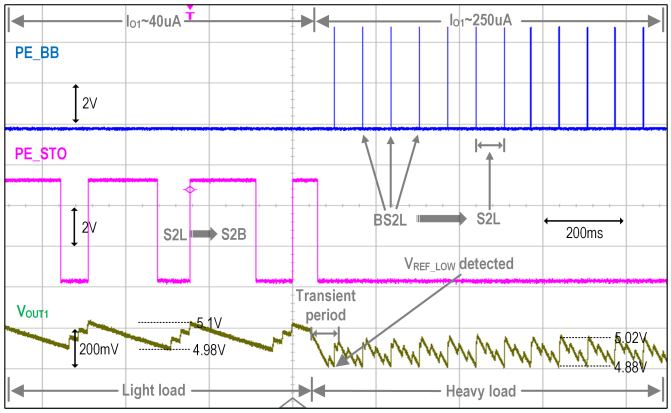

Fig. 24. Measured V_{OUT1} regulation with different loads.

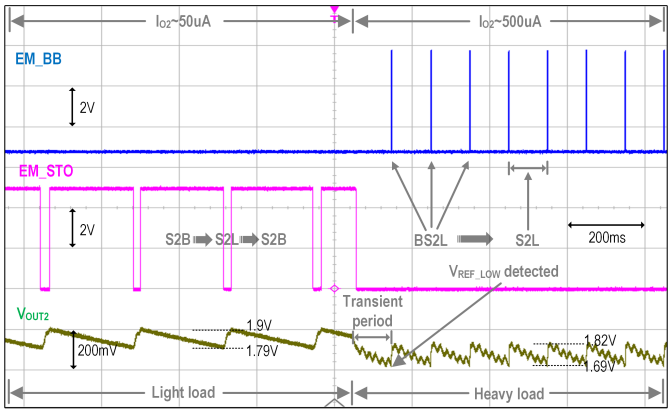

Fig. 25. Measured V_{OUT2} regulation with different loads.

harvester is mounted on a shaker and excited by an amplified ac vibration signal.

Fig. 20 shows the measured open-circuit voltages from the PE harvester ($V_{OC,PE}$) and the EM harvester (V_{EM}), verifying that $V_{OC,PE}$ lags V_{EM} by 90 degrees, consistent with the analytical model in Section II-B. Fig. 21 demonstrates that PE bias-flipping is strictly time-interleaved with EM harvesting at the EM current zero-crossing points, aligning with the expected phase relationship. The signal *BF* indicates the bias-flip event.

The mode-transition waveform of the PE rectifier switching between S2L and S2B modes is shown in Fig. 22. The output V_{OUT1} is regulated within the designated hysteresis window, and the system's maximum voltage V_{MAX}, also labeled V_{DD} in Fig. 17, tracks V_{OUT1}, which at this time is the system's highest voltage. The SSHI rectifier achieves a 71% voltage bias-flip efficiency using the shared EM coil. Fig. 23 illustrates the corresponding mode transitions in the EM rectifier. The multi-step rectifier is driven by the on-chip clock (CLK), and the spikes in the signal I_{COIL} confirm that bias-flipping occurs precisely at the EM current zero crossing.

Figs. 24 and 25 display the system output regulation waveforms with different loads. It can be observed that under light load, the system switches between S2L and S2B modes,

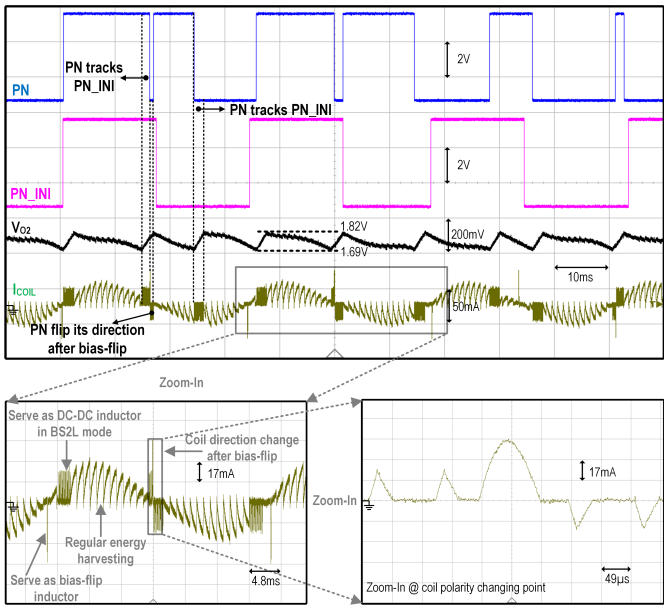

Fig. 26. Measured timing diagram for proposed coil-direction arbit algorithm and transient coil current under heavy load.

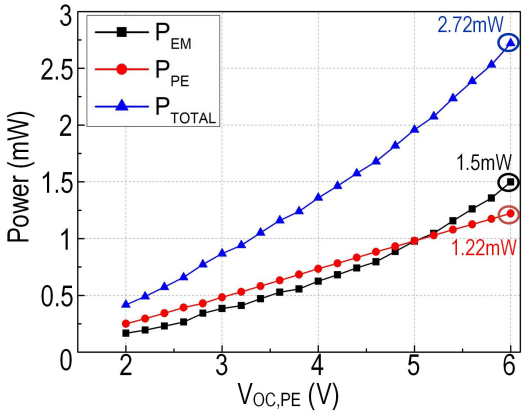

Fig. 27. Measured output power versus different $V_{OC,PE}$.

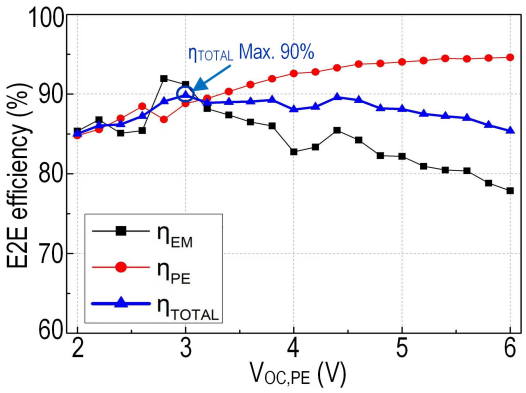

Fig. 28. Measured end-to-end efficiency versus different $V_{OC,PE}$.

and the two outputs are regulated in the upper hysteresis window, from 4.98 to 5.1 V for V_{OUT1} and from 1.79 to 1.9 V for V_{OUT2}. The signal PE(EM)_STO (PE_STO or EM_STO) flags the mode switching between S2L (PE(EM)_STO = 0) and S2B (PE(EM)_STO = 1) during light load, while the signal PE(EM)_BB flags the mode switching between S2L (PE(EM)_BB = 0) and BS2L (PE(EM)_BB = 1) under heavy load. In these two figures, during the transient periods from light to heavy load, the system enters BS2L mode when the outputs drop below V_{REF}. Then, the outputs will be regulated in the lower hysteresis window, between 4.88 and 5.02 V for V_{OUT1} and between 1.69 and 1.82 V for V_{OUT2}. The power consumption during regular operation in S2L/S2B mode is 4.1 μW, whereas in heavy-load BS2L mode it increases to 15 μW due to the activation of the higher-frequency 10-kHz dc–dc conversion.

Fig. 26 verifies the effectiveness of the coil-direction judgment algorithm and the proposed CPM technique under heavy load conditions. The comparator CMP_PN, as shown in Fig. 12, determines the coil current direction during S2L mode by comparing the voltages at the two terminals of the coil. Once one of the output voltages reaches its corresponding V_{REF}, the system transitions into BS2L mode. At this point, the comparator outputs the initial polarity signal PN_INI to the direction arbiter and subsequently powers down to conserve energy. As shown in Fig. 26, the signal *PN* tracks PN_INI until a bias-flip event is detected. After the flip, *PN* switches to the opposite state, indicating a change in coil current direction and thus triggering the appropriate dc–dc path. The zoomed-in-view waveform of the coil current clearly demonstrates the time-interleaved behavior of the coil as it is dynamically shared across three roles: EM energy source, PE bias-flipping inductor, and dc–dc conversion inductor. The zoomed-in-view sub-figure at the bottom right illustrates that bias-flipping is given higher priority than dc–dc operation, thereby avoiding conflicts.

Fig. 27 shows the measured output power under varying external excitation levels ($V_{OC,PE}$), including contributions from the PE and EM sources individually, as well as the combined total output of the proposed energy harvesting platform. The system achieves a maximum output power of 2.72 mW, with 1.5 and 1.22 mW contributed by the EM and PE harvesters, respectively. Under weak excitation, the PE harvester contributes a larger share of the total power; as the excitation level increases, the EM harvester becomes the dominant source.

The measured end-to-end (E2E) energy efficiency for the two individual outputs and the combined hybrid operation is shown in Fig. 28. The proposed system achieves a peak combined E2E efficiency of 90%, and maintains over 85% across the full measured $V_{OC,PE}$ range from 2 to 6 V. For the PE energy extraction path, efficiency continues to increase with higher excitation levels, as the relative impact of voltage drop across the NVC diminishes at higher $V_{OC,PE}$. In contrast, the EM energy extraction path exhibits different trends: at low input excitation levels, efficiency is primarily limited by switch-driving and control losses; at high excitation levels, conduction losses in the EM rectifier during the current

TABLE II
COMPARISON TABLE OF THE PROPOSED COIL-SHARING IC WITH PRIOR STATE-OF-THE-ART DESIGNS

	JSSC'17 [15]	TCAS1'19 [16]	ISSCC'20 [26]	ISSCC'22 [21]	JSSC'23 [6]	JSSC'23 [20]	**This work**
Technology	350 nm	180 nm	600 nm	65 nm	180 nm	180 nm	180 nm
Technique	Conduction Angle	Energy Investment	Constant ZHAR	MSVR SECE	DCB-SSHI	Multi-source stack	**Coil-Sharing**
Harvester Type	EM	PE+EM	EM	PE/TEG/PV	PE	2*PE/TEG/PV	**PE+EM**
C_P (nF)	N/A	9	N/A	N/A	42	100	**440**
Frequency (Hz)	64.4	PE:500 EM:20	50	N/A	230	25	**30**
Cascaded Stage	3	2	1	1	2	3	**1**
Output Regulation?	Yes	No	No	Yes	No	No	**Yes(1.8V, 5V)**
Fully Integrated?	No	No	Yes	No	No	No	**Yes**
E2E Efficiency	95%	90%(hybrid)	98.8%	80%(hybrid)	N/A	78.8%	**90%(hybrid)**
Passive Component for Bias-Flip	No Bias-Flip	No Bias-Flip	No Bias-Flip	L=22μH	L=120μH	No Bias-Flip	**None**
Passive Component for DC-DC	L=3.3mH	L=3.3mH	No Regulation	L=22μH	L=120μH	L=470μH	**None**
Normalized V_{NOR}	34	34	1	1.22	2.2	5.7	**1**
Max. Output Power	1.2mW	0.1mW	N/A	1.2mW	0.27mW	5mW	**2.72mW**
MOPIR (PE)	N/A	1.48×	N/A	3.2×	7.38×	2.3×	**4.7×**

N/A: Not reported.

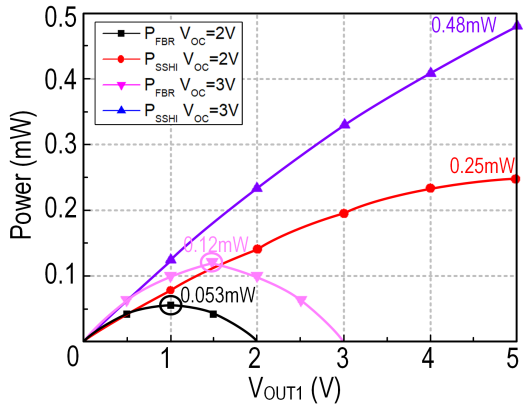

Fig. 29. Measured PE extracted power compared with FBR.

integration phase become dominant, resulting in a gradual decrease in E2E efficiency as $V_{OC,PE}$ increases.

Fig. 29 highlights the measurement results focused on the PE energy extraction capability. It compares the measured PE output power under different V_{OUT1} values with that of an ideal FBR. At $V_{OC,PE}$ = 2 V, the proposed SSHI rectifier delivers up to 0.25 mW, achieving a maximum output power improvement ratio (MOPIR) of 4.7× compared with a typical FBR, which outputs only 0.053 mW. When $V_{OC,PE}$ increases to 3 V, the improvement becomes 4×, from 0.12 mW (FBR) to 0.48 mW (SSHI). This trend arises because, at higher $V_{OC,PE}$ levels, the maximum power point (MPP) of the PE rectifier shifts beyond the breakdown voltage limit of on-chip devices (approximately 5 V). As a result, the practically achievable output power becomes constrained and falls short of the theoretical maximum.

Table II lists the comparison of the proposed coil-sharing hybrid energy harvesting platform with prior state-of-the-art designs. Unlike previous works, this design eliminates the need for any on-chip or off-chip inductors or capacitors for PE voltage bias-flipping or power conversion, while still supporting dual-regulated outputs. This approach saves both physical space and material cost. To quantitatively evaluate the compactness of the proposed circuit-level interface, and following the methodology in previous works [10], [14], we assume an inductor size of 100 mm^3/mH, a capacitor size of 0.75 mm^3/unit, and a chip volume of 10 mm^3. Based on these values, the normalized volume V_{NOR} is defined as follows:

$$V_{NOR} = \frac{\text{Total Interface Circuit Volume}}{\text{Chip Volume}}. \tag{4}$$

Benefiting from a single-stage energy transfer topology, with no more than two power transistors in any conduction path, the system achieves a peak end-to-end (E2E) efficiency of 90%. For the PE energy harvesting path specifically, an MOPIR of 4.7× is realized.

VI. CONCLUSION

By properly using the in-phase relationship between PE and EM energy sources in the hybrid energy harvester, this work introduced a novel coil-sharing energy harvesting platform. Due to the proper time-interleaving arrangement, the coil can serve as either an active energy source or a passive inductor for PE voltage bias-flipping, dc–dc conversion, and output regulation. It first achieves the fully integrated operation in the hybrid energy harvesting. The decreased system volume and high output power satisfy the power requirement in volume-constrained IoT wireless sensors.

REFERENCES

[1] P. D. Mitcheson, E. M. Yeatman, G. K. Rao, A. S. Holmes, and T. C. Green, "Energy harvesting from human and machine motion for wireless electronic devices," *Proc. IEEE*, vol. 96, no. 9, pp. 1457–1486, Sep. 2008.

[2] P. Mayer, M. Magno, and L. Benini, "Energy-positive activity recognition—From kinetic energy harvesting to smart self-sustainable wearable devices," *IEEE Trans. Biomed. Circuits Syst.*, vol. 15, no. 5, pp. 926–937, Oct. 2021.

[3] Y. K. Ramadass and A. P. Chandrakasan, "An efficient piezoelectric energy harvesting interface circuit using a bias-flip rectifier and shared inductor," *IEEE J. Solid-State Circuits*, vol. 45, no. 1, pp. 189–204, Jan. 2010.

[4] Y.-W. Jeong, S.-J. Lee, and S.-U. Shin, "A scalable N-step equally split SSHI rectifier for piezoelectric energy harvesting with low-Q inductor," *IEEE J. Solid-State Circuits*, vol. 58, no. 12, pp. 3519–3529, Dec. 2023.

[5] S. Jiang, X. Yue, Y. Ma, C. Wang, and S. Du, "A rectifier-less piezoelectric energy-harvesting interface with a sense & track MPPT achieving single-cycle convergence and 568% shock power improvement," in *IEEE Int. Solid-State Circuits Conf. (ISSCC) Dig. Tech. Papers*, Feb. 2025, pp. 522–524.

[6] X. Yue, S. Javvaji, Z. Tang, K. A. A. Makinwa, and S. Du, "A bias-flip rectifier with duty-cycle-based MPPT for piezoelectric energy harvesting," *IEEE J. Solid-State Circuits*, vol. 59, no. 6, pp. 1771–1781, Jun. 2024.

[7] M. Shim, J. Kim, J. Jeong, S. Park, and C. Kim, "Self-powered 30 μW to 10 mW piezoelectric energy harvesting system with 9.09 ms/V maximum power point tracking time," *IEEE J. Solid-State Circuits*, vol. 50, no. 10, pp. 2367–2379, Oct. 2015.

[8] X. Yue and S. Du, "A single-stage bias-flip regulating rectifier with fully digital duty-cycle-based MPPT for piezoelectric energy harvesting," *IEEE J. Solid-State Circuits*, vol. 60, no. 3, pp. 850–860, Mar. 2025.

[9] S. Li, A. Roy, and B. H. Calhoun, "A piezoelectric energy-harvesting system with parallel-SSHI rectifier and integrated MPPT achieving 417% energy-extraction improvement and 97% tracking efficiency," in *Proc. Symp. VLSI Circuits*, Jun. 2019, pp. C324–C325.

[10] S. Du and A. A. Seshia, "An inductorless bias-flip rectifier for piezoelectric energy harvesting," *IEEE J. Solid-State Circuits*, vol. 52, no. 10, pp. 2746–2757, Oct. 2017.

[11] Z. Chen, M.-K. Law, P.-I. Mak, X. Zeng, and R. P. Martins, "Piezoelectric energy-harvesting interface using split-phase flipping-capacitor rectifier with capacitor reuse for input power adaptation," *IEEE J. Solid-State Circuits*, vol. 55, no. 8, pp. 2106–2117, Aug. 2020.

[12] S. Du, Y. Jia, C. Zhao, G. A. J. Amaratunga, and A. A. Seshia, "A fully integrated split-electrode SSHC rectifier for piezoelectric energy harvesting," *IEEE J. Solid-State Circuits*, vol. 54, no. 6, pp. 1733–1743, Jun. 2019.

[13] X. Yue and S. Du, "A synchronized switch harvesting rectifier with reusable storage capacitors for piezoelectric energy harvesting," *IEEE J. Solid-State Circuits*, vol. 58, no. 9, pp. 2597–2606, Sep. 2023.

[14] Z. Li et al., "Piezoelectric energy harvesting interface using self-bias-flip rectifier and switched-PEH DC–DC for MPPT," *IEEE J. Solid-State Circuits*, vol. 59, no. 7, pp. 2248–2259, Jul. 2023.

[15] J. Leicht and Y. Manoli, "A 2.6 μW–1.2 mW autonomous electromagnetic vibration energy harvester interface IC with conduction-angle-controlled MPPT and up to 95% efficiency," *IEEE J. Solid-State Circuits*, vol. 52, no. 9, pp. 2448–2462, Sep. 2017.

[16] S. Chamanian, B. Çiftci, H. Ulusan, A. Muhtaroglu, and H. Külah, "Power-efficient hybrid energy harvesting system for harnessing ambient vibrations," *IEEE Trans. Circuits Syst. I, Reg. Papers*, vol. 66, no. 7, pp. 2784–2793, Jul. 2019.

[17] S. Jia et al., "A self-powered interface circuit for simultaneous piezoelectric and electromagnetic energy extraction," *IEEE Trans. Power Electron.*, vol. 38, no. 9, pp. 10640–10650, Sep. 2023.

[18] Z. Xie, L. Teng, H. Wang, Y. Liu, M. Fu, and J. Liang, "A self-powered synchronous switch energy extraction circuit for electromagnetic energy harvesting enhancement," *IEEE Trans. Power Electron.*, vol. 38, no. 8, pp. 9972–9982, Aug. 2023.

[19] Z.-Y. Yang et al., "A 93.2%-efficiency multi-input bipolar energy harvester with 17.9× MPPT loss reduction," in *IEEE Int. Solid-State Circuits Conf. (ISSCC) Dig. Tech. Papers*, Feb. 2023, pp. 440–442.

[20] X. Wang et al., "Configurable hybrid energy synchronous extraction interface with serial stack resonance for multi-source energy harvesting," *IEEE J. Solid-State Circuits*, vol. 58, no. 2, pp. 451–461, Feb. 2023.

[21] S. Li, X. Liu, and B. H. Calhoun, "A 32 nA fully autonomous multi-input single-inductor multi-output energy-harvesting and power-management platform with 1.2×105 dynamic range, integrated MPPT, and multi-modal cold start-up," in *IEEE Int. Solid-State Circuits Conf. (ISSCC) Dig. Tech. Papers*, vol. 65, Feb. 2022, pp. 1–3.

[22] S. S. Amin and P. P. Mercier, "MISIMO: A multi-input single-inductor multi-output energy harvester employing event-driven MPPT control to achieve 89% peak efficiency and a 60,000× dynamic range in 28 nm FDSOI," in *IEEE Int. Solid-State Circuits Conf. (ISSCC) Dig. Tech. Papers*, Feb. 2018, pp. 144–146.

[23] C. J. Lukas et al., "A 2.19 μW self-powered SoC with integrated multimodal energy harvesting, dual-channel up to -92 dBm WRX and energy-aware subsystem," in *IEEE Int. Solid-State Circuits Conf. (ISSCC) Dig. Tech. Papers*, Feb. 2023, pp. 238–240.

[24] Y. Wei, X. Yue, Z. Chen, and S. Du, "31.1 an inductor-less capacitor-less synchronous piezoelectric-electromagnetic hybrid energy harvesting platform with coil-sharing scheme," in *IEEE Int. Solid-State Circuits Conf. (ISSCC) Dig. Tech. Papers*, Feb. 2025, pp. 1–3.

[25] S. Du, Y. Jia, C. Zhao, G. A. J. Amaratunga, and A. A. Seshia, "A passive design scheme to increase the rectified power of piezoelectric energy harvesters," *IEEE Trans. Ind. Electron.*, vol. 65, no. 9, pp. 7095–7105, Sep. 2018.

[26] A. Quelen, G. Pillonnet, P. Gasnier, F. Rummens, and S. Boisseau, "32.3 electromagnetic mechanical energy-harvester IC with no off-chip component and one switching period MPPT achieving up to 95.9% end-to-end efficiency and 460% energy-extraction gain," in *IEEE Int. Solid-State Circuits Conf. (ISSCC) Dig. Tech. Papers*, Feb. 2020, pp. 490–492.

[27] X. Yue and S. Du, "A single-stage bias-flip regulating rectifier with fully-digital fast-MPPT for piezoelectric energy harvesting achieving 9.3× power enhancement and 92.5% end-to-end efficiency," in *Proc. IEEE Custom Integr. Circuits Conf. (CICC)*, Apr. 2024, pp. 1–2.

[28] X. Yue, S. Javvaji, Z. Tang, K. A. A. Makinwa, and S. Du, "A bias-flip rectifier with a duty-cycle-based MPPT algorithm for piezoelectric energy harvesting with 98% peak MPPT efficiency and 738% energy-extraction enhancement," in *IEEE Int. Solid-State Circuits Conf. (ISSCC) Dig. Tech. Papers*, Feb. 2023, pp. 442–444.

Yuchen Wei received the B.Sc. degree from the University of Electronic Science and Technology of China (UESTC), Chengdu, China, in 2022, and the M.Sc. degree (Hons.) from the Department of Microelectronics, Electronic Instrumentation Laboratory, Delft University of Technology (TU Delft), Delft, The Netherlands, in 2024.

His current research interests include power management integrated circuits and analog integrated circuits.

Xinling Yue (Graduate Student Member, IEEE) is currently pursuing the Ph.D. degree in microelectronics with the Electronic Instrumentation Laboratory, Delft University of Technology, Delft, The Netherlands.

She joined the Electronic Instrumentation Laboratory, Delft University of Technology, in December 2020. Her current research interests are energy-efficient power management integrated circuits and systems, which include energy harvesting, ac/dc rectifiers, dc/dc converters, and maximum power point tracking techniques.

Ms. Yue received the Best Student Paper Award at the 2022 IEEE International Conference on Electronics Circuits and Systems (ICECS) and the Student Travel Grant Awards at the 2022 IEEE International Symposium on Circuits and Systems (ISCAS) and 2023 International Solid-State Circuits Conference (ISSCC).

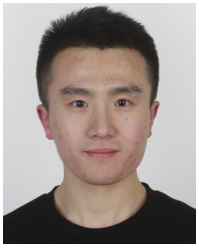

Tianqi Lu (Graduate Student Member, IEEE) received the B.Sc. degree in physics from Nanchang University, Nanchang, China, in 2018, and the M.Sc. degree in integrated circuit engineering from Tsinghua University, Beijing, China, in 2021. He is currently pursuing the Ph.D. degree with the Department of Microelectronics, Delft University of Technology, Delft, The Netherlands.

His research interests include power-management/mixed-signal integrated circuits for wireless power transfer systems, dc–dc power converters, and biomedical applications.

Zhiyuan Chen (Member, IEEE) received the B.Sc., M.Sc., and Ph.D. degrees from the University of Macau (UM), Macau, China, in 2011, 2013, and 2018, respectively.

Since 2018, he has been with Fudan University, Shanghai, China, where he is currently an Associate Professor. His research interests include ac–dc rectifiers, dc–dc converters, and energy harvesting systems.

Dr. Chen serves as a member for the Technical Committee on Power and Energy Circuits and Systems in the IEEE Circuits and Systems Society. He has been a Review Committee Member for IEEE International Symposium on Circuits and Systems since 2021. He was a recipient of Macau Science and Technology Development Fund (FDCT) Postgraduate Award and Shanghai Super Postdoctoral Award.

Sijun Du (Senior Member, IEEE) received the B.Eng. degree (Hons.) in electrical engineering from the University Pierre and Marie Curie (UPMC), Paris, France, in 2011, the M.Sc. degree (Hons.) in electrical and electronic engineering from the Imperial College, London, U.K., in 2012, and the Ph.D. degree in electrical engineering from the University of Cambridge, Cambridge, U.K., in January 2018.

He was with the Laboratoire d'Informatique de Paris 6 (LIP6), UPMC, and then worked as an IC Engineer in Shanghai, China, from 2012 to 2014. He was a summer Engineer Intern with Qualcomm Technology Inc., San Diego, CA, USA, in 2016. He was a Post-Doctoral Researcher with the Department of Electrical Engineering and Computer Sciences (EECS), University of California at Berkeley, Berkeley, CA, USA, from 2018 to 2020. In 2020, he joined the Department of Microelectronics, Delft University of Technology (TU Delft), Delft, The Netherlands, as an Assistant Professor. His current research is focused on energy-efficient integrated circuits and systems, including power management integrated circuits (PMICs), energy harvesting, wireless power transfer, and dc/dc converters.

Dr. Du received the Dutch Research Council (NWO) Talent Program VENI Grant in the 2021 round, the Best Student Paper Award at IEEE ICECS 2022, and the SSCS Reviewer Award in 2024. He serves as a Technical Program Committee (TPC) Member for IEEE ISSCC, ISSCC ESSERC, and ISSCC Student Research Preview (SRP). He served as the Sub-Committee Chair for IEEE ICECS in 2022 and 2024. He has been serving as the Sub-Committee Chair for IEEE ISCAS since 2025.